Clay platelet orientation inside self-standing beidellite clay films: Effect of silica nanospheres and link with macroscopic mechanical resistance

Sivagen Vydelingum, Pierre Levitz, Laurent J Michot, Thomas Bizien, Pierre Rabu, Ovidiu Ersen, Thibaud Chevalier, Natalie Malikova

Clay platelet orientation inside self-standing beidellite clay films: effect of silica nanospheres and link with macroscopic mechanical resistance

Sivagen Vydelingum[a, b, c], Pierre Levitz[a], Laurent J. Michot[a], Thomas Bizien[d], Pierre Rabu[b], Ovidiu Ersen[b], Thibaud Chevalier[c] and Natalie Malikova[a]

[a]PHENIX Laboratory, UMR 8234 CNRS, Sorbonne University, 75005, Paris, France

[b]IPCMS Laboratory, UMR 7504 CNRS, University of Strasbourg, 67200, Strasbourg, France

[c]IFP Energies nouvelles, 1 et 4 avenue de Bois-Préau, 92852 Rueil-Malmaison, France

[d]Synchrotron SOLEIL, l'Orme des Merisiers, 91190, Saint-Aubin, France

Corresponding author(s):

sivagen.vydelingum@sorbonne-universite.fr; natalie.malikova@sorbonne-universite.fr

Highlights

- Self-standing films of clay platelets and nanospheres were produced.
- Platelet orientation in the films was investigated by SAXS.
- Clay ordering within films is favoured for small platelets.
- Sphere-clay interactions modulate the tensile strength of films.

Abstract

Clay minerals and silica are essential components of soil. Understanding the multi-scale structure of a simple model system formed of (negatively charged) beidellite clay nanoplatelets and silica nanospheres is a first step in understanding the complex structure of soil. Due to their strong shape anisotropy, clay nanoplatelets exhibit preferential orientation at the microscopic level, both in aqueous dispersions and in dry deposits. Adding spherical colloids into the system changes the clay platelet organisation. These changes are studied here for the case of self-standing clay films, using a small angle X-ray scattering (SAXS) beamline, equipped with a goniometer and a rotating device. We investigated orientation of clay nanoplatelets as a function of the nanoplatelet and nanosphere sizes, their surface charge and sphere/platelet number ratio. Two methodologies are developed to calculate the nanoplatelet order parameter $\langle P_2 \rangle$: (a) background contribution is subtracted from the azimuthal profile curve at a given wavevector q and (b) isotropic contribution is subtracted directly at the level of the 2D SAXS images. Smaller clay nanoplatelets (~200nm in lateral size) exhibit a better orientation than larger platelets (> ~300nm). Adding small positively and negatively charged nanospheres (diameter ~ 30nm) destroys the high degree of orientation of small clay platelets. Large spheres (diameter similar to the nanoplatelet size, ~300nm) destroy orientation for both types of clay platelets. A simple tensile strength setup allows to measure the breaking stress of the self-standing films to make the link between microscopic and macroscopic structure. Films of small clay platelets without spheres were mechanically the most resistant. Films with added positively charged spheres were stiffer than films with negatively charged spheres. The methodology presented here opens perspectives for the study of structure and mechanical response of clay deposits.

Keywords: clay nanoplatelets, silica nanospheres, self-standing films, SAXS, orientation, tensile strength

1. Introduction

Natural soils are complex multi-scale assemblies of inorganic, organic and biological components. The organization of the various soil components plays a major role in the functioning of the whole system and controls to a large extent the fertility, stability and degradation of soils. Among the various soil constituents, clay minerals are of prime importance and clay content is indeed a key factor in soil taxonomy (Soil Survey Staff. 1999). These minerals are layered materials with unique properties such as high surface area, water retention, ion exchange capacity and fixation of organic matter (Velde, 1992; Bergaya et al., 2006). Due to these properties, they play a major role in soil functioning and control to a large extent plant nutrition, water retention, transport and mechanical strength. This is directly related to the microstructure resulting from the association of clays with other soil components such as silts and sands. This generates various assemblies that have been studied extensively (e.g. Stoops and Jongerius, 1975; Fiès and Stengel, 1984; Bruand and Prost, 1987, 1988; Bruand et al., 1988.; Attou et al., 1998; Rozenbaum et al., 2012). In that context, developing a model system mimicking the association of silts and clays could provide relevant information on the pertinent parameters affecting microstructure by analyzing in detail the multi-scale organization of these two components in the solid state.

The model system investigated is composed of size-sorted Na-exchanged beidellite clay particles (the swelling component of soil) and silica spheres (the silts). The behavior of aqueous suspensions of beidellite platelets has been studied in detail (Paineau et al., 2009, 2011) and reveals the existence of an Isotropic/Nematic phase transition occurring before the sol/gel

transition. These features are slightly modified upon addition of colloidal spheres(Hilhorst et al., 2014; Landman et al., 2014; Bailey et al., 2015), which reveals the presence of interactions between both components in the system. For an equivalent system with gibbsite platelets and silica nanospheres enhanced density fluctuations were observed (Doshi et al., 2011). However, how these interactions affect the structure of films formed from these colloidal mixtures remains to be analyzed. To shed new light on this issue, in the present work we varied the size of both clay nanoplatelets and silica nanospheres, as well as the relative proportions of both components. In addition, for modifying the interactions in the mix, as clay particles are negatively charged (Bergaya et al., 2006) we used classical silica spheres that are negatively charged at neutral pH, and alumina coated silica spheres that display an isoelectric point around 8 and can then be positively charged for lower pH values.

In this manuscript we focus on the effect of nanosphere component on the orientational features of clay nanoplatelets in composite self-standing films, which may be relevant in the context of soil degradation by crusting. In a very recent study the orientation of clay phases in real soil samples was investigated using synchrotron-based microdiffraction experiments and it was shown that the presence of coarse quartz grains had a significant effect on clay orientation in the crusts (Geoffroy et al., 2022). In our approach, we developed a rotating device in order to analyze in detail, using SAXS, the evolution of clay anisotropy in dry self-standing films formed with various ratios of different spheres and platelets. Using a recently developed orientation distribution function (ODF) (Dabat et al., 2019, 2020), we examine how the various parameters of the initial suspension affect the orientation of clay platelets in the film. Indeed, even if Maier-Saupe ODF is usually used for platelet system, it is not able to fit experimental data for clay systems at low and high order parameter values (Dabat et al., 2019). The new generalized ODF for clay systems is able to fit the whole range of order parameter. In parallel, using a recently developed tensile strength setup (Carrier et al., 2016,) we examine the potential

relationships between clay orientation in the films extracted from SAXS measurements and mechanical strength of the film at the macroscopic scale.

2. Materials and methods

2.1 Sample preparation

2.1.1 Clay size sorting and purification

Beidellite SBId-1 from Idaho with an average structural formula that can be written as $(Si_{7.27}Al_{0.73})(Al_{3.77}Fe^{3+}_{0.11}Mg_{0.21})O_{20}(OH)_4Na_{0.67}$) was purchased from the Source Clays Minerals Repository of Clay Minerals Society (Purdue University). Prior to use, beidellite natural clay was sodium exchanged, purified and size sorted according to previously established procedures (Michot et al., 2004; Paineau et al., 2011). Table 1 presents the size and charge characteristics of the two sizes of beidellite used in the present study (Paineau et al., 2011).

Table.1: Beidellite platelet characteristics: Average lateral size, average thickness, polydispersity and CEC.

Size fraction	S1	S3
Lateral size (nm)	330	210
Polydispersity diameter (%)	47	38
CEC (meq/100g)	64.2	94.3

Thickness of size fraction S1 and S3 platelets is around 1 nm. Presence of kaolin particles in size fraction S1 explains a CEC value low as $64.2\ meq/100g$. Regarding S3 CEC slightly higher value than expected from structural formula is mostly due to the platelets small size and the charges of platelet edge taken into account in CEC value.

129 2.1.2 Silica spheres

130 Small silica spheres: ludox TM-50 was purchased from Sigma-Aldrich (30 nm in diameter)
131 and ludox CL-P was purchased from Grace (28 nm in diameter). Large silica spheres: silica
132 spheres were purchased from cospheric (CS) and from Creative diagnostics (CD) (both 300 nm
133 in diameter). Both Ludox CL-P and CD spheres are coated by Al_2O_3 and then bear a positive
134 charge surface for pH values ≤ 6 (Supplementary info 1). The zeta potential of beidellite
135 platelets is around -40 mV over the whole pH range (Housni et al., 2020). Ludox TM-50 and
136 cospheric spheres were used at pH 8 and are then negatively charged whereas Ludox CL-P and
137 CS were used at pH 4 where they bear a positive surface charge (Table 2). Charge densities for
138 the different spheres are of similar value and only of opposite charge (Supplementary info 1).

139 **Table. 2**: Sphere characteristics: diameter, pH used for deposit and charge surface.

	Ludox TM-50	Ludox CL-P	Cospheric silica	CD silica
Diameter (nm)	30	28	300	300
pH used for deposit	8	4	8	4
Surface charge at pH used	(-)	(+)	(-)	(+)

140

141 2.1.3 Self-standing films

142 Aqueous suspensions of clay platelets and silica spheres are mixed to produce suspensions
143 of different sphere/platelet nominal number ratios (R_n) given by the following equation:

144 $$R_n = \frac{N_s}{N_p} \quad (1)$$

145 Where N_s is the number of spheres and N_p the number of platelets per unit volume. Mixed
146 sphere/platelet dispersions are deposited onto an aluminium cup and dried at room temperature
147 to form self-standing films. Self-standing films of a few tenths of micrometers in thickness are

recovered. For large spheres, the number ratios used for small spheres do not yield self-standing films. Therefore, a surface ratio is used instead of a number ratio, according to:

$$R_s = R_n \frac{8R^2}{d^2} \quad (2)$$

where d is the platelet lateral size and R the sphere radius. The sequence of films produced is summarized in Table 3. Number ratio R_n is chosen in order to understand sphere-platelet interactions by varying their relative number. Compared to this, the surface ratio R_s helps to estimate the number of platelets needed to cover the surface of a large sphere.

Figure 1 presents TEM images of mixed platelet-sphere deposits. To produce TEM compatible deposits (maximum thickness of 100nm), mixed suspensions of platelets and spheres at a required ratio were deposited on TEM grids and left to evaporate. Both spheres and platelets can be easily distinguished in the images. TEM image with positive spheres (Figure 1a) displays a relatively homogeneous mix of the two components and no phase separation. Most of the positive spheres are on the lateral surface of the platelets and only a few are close to platelet edges. Several layers of clay platelets can be seen on the image. The image with negative spheres (Figure 1b) presents areas of phase separation of the two components, spheres are located mainly on platelet edges. Figure 2 presents SEM images of the mixed self-standing films (a few tens of μm thick). S1 beidellite self-standing films without spheres (Figure. 2a) display a weaker clay platelet alignment compared to S3 beidellite films without spheres (Figure 2b). The clay platelet alignment is even weaker for composite films of S3 beidellite with large positively charged spheres (Figure 2c).

Table. 3: Number and surface ratios, R_n and R_s, used for small and large spheres to produce self-standing films.

171

Deposits with small spheres R_n	Deposits with large spheres		
	R_n	R_s equivalent (S1 platelets)	R_s equivalent (S3 platelets)
0.3	0.002	0.003	0.009
1.0	0.005	0.008	0.022
3.0	0.016	0.026	0.072

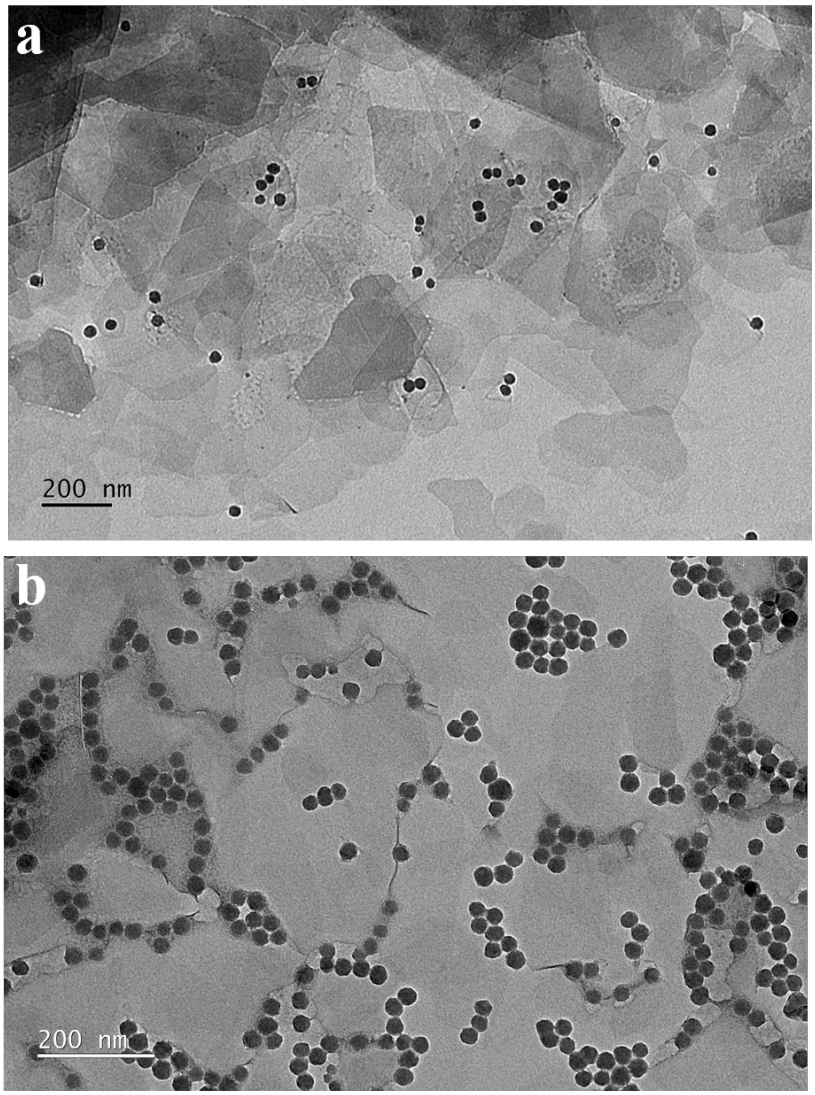

172

173 **Figure. 1** : TEM images of beidellite clay platelets mixed with silica spheres. TEM projections
174 images at 0°. (a) S1 beidellite (lateral size 330 nm) mixed with ludox CL-P (positively charged
175 small spheres, diameter 28 nm) at $R_n = 0.3$. Image size: 4008x2642. (b) S3 beidellite (lateral
176 size 210 nm) mixed with ludox TM-50 (negatively charged small spheres, diameter 30 nm) at
177 $R_n = 2$. Image size: 4008x2642.

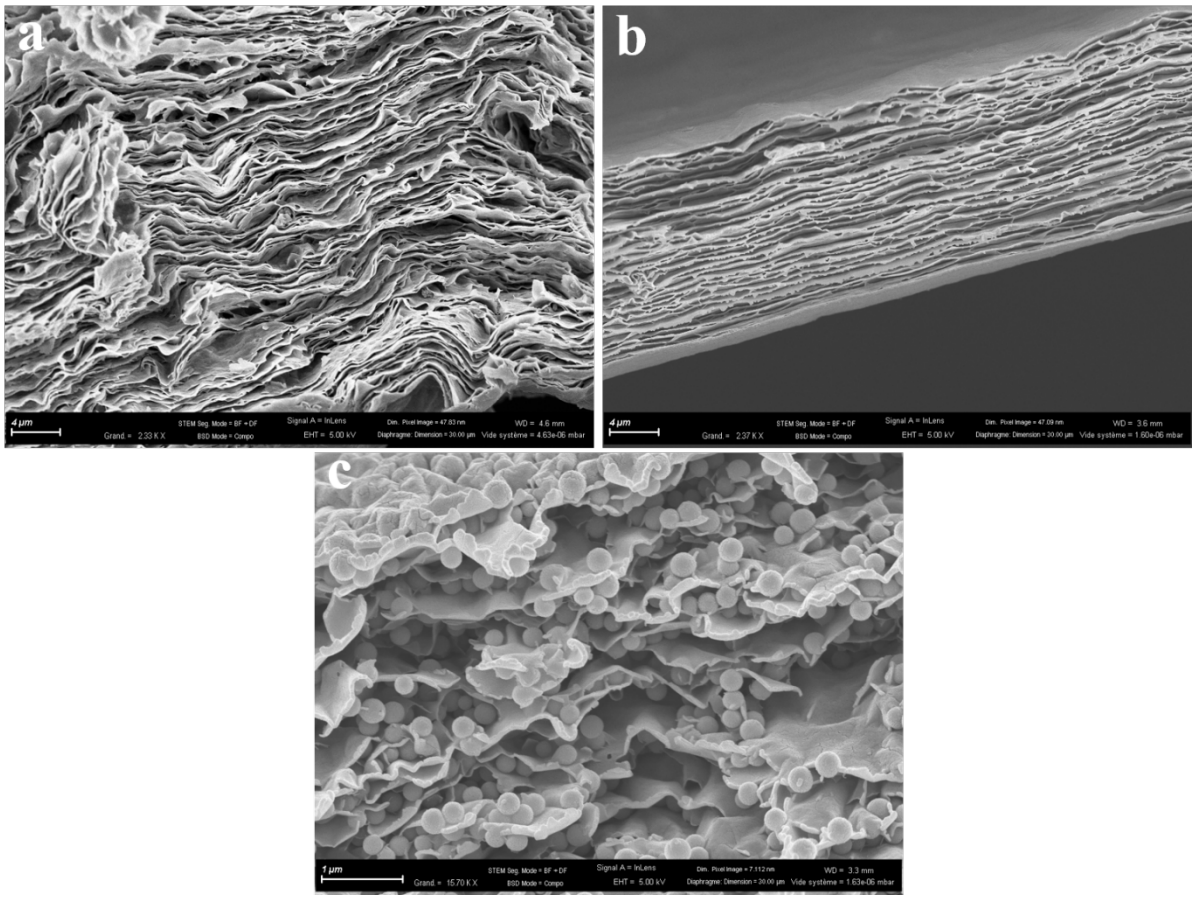

178

179 **Figure. 2** : SEM images of self-standing films of beidellite clay platelets mixed with silica
180 spheres. (a) S1 beidellite (lateral size 330 nm) without spheres. (b) S3 beidellite (lateral size
181 210 nm) without spheres. (c) S3 beidellite mixed with CD silica (positively charged large
182 spheres, diameter 300 nm).

183 ## 2.2 Small Angle X-ray Scattering

184 ### 2.2.1 Beamline setup

185 SAXS experiments were conducted at SOLEIL synchrotron on beamline SWING at a fixed
186 energy of 12 keV, i.e. a fixed wavelength of 1 Å and two sample-to-detector distances (0.5 m
187 and 6 m). Hence, the available q range varied from 0.002 $Å^{-1}$ to 2 $Å^{-1}$ ($q = \frac{4\pi(sin\theta)}{\lambda}$, where
188 2θ is the scattering angle and λ the X-ray wavelength). 2D scattering signal was collected on
189 an Eiger 4M detector.

190 2.2.2 Goniometer and rotating device

191 A goniometer and a rotating device were installed onto the SAXS beamline. Using a razor,
192 clay films were cut into slabs (an approximate shape of a rectangular cuboid, slab thickness of
193 the order of 100 µm, length of several mm). The slabs were glued to a needle's top
194 (Supplementary info 2). The needle itself was glued to a small copper piece which was inserted
195 into the goniometer head. The goniometer allowed adjusting the slab orientation in the vertical
196 direction. The entire set-up (including the goniometer head) was then allowed to rotate and
197 SAXS patterns were collected at different rotation angles, which enables defining properly
198 sample orientation to determine the anisotropy of clay platelets inside the film (Figure 3).

199

200 2.3 Tensile strength measurement

201 A setup developed by (Carrier et al., 2016) was used to perform tensile strength
202 measurements on self-standing films cut into a specific form to allow an equal load distribution
203 on the film (Supplementary info 3). Breaking stress measurements were performed by gradually
204 increasing the stress on the film (a bottle fixed by a thread to the setup was gradually filled with
205 water). Film deformation was not investigated during the experiment. Breaking stress σ was
206 estimated by the following equation:

207 $$\sigma = \frac{mg}{S} \quad (3)$$

208 Where m corresponds to the mass of water present in the bottle necessary to split the film, S is
209 the film's surface under stress. Tensile strength measurements were made in the following range
210 of relative humidity (RH) and temperature: $RH = 20 - 24\%$, $T = 19.4 - 21.6\,°C$. As
211 reported by (Carrier et al., 2016), *RH* has a significant influence on the mechanical resistance
212 of self-standing films. In the present case, by working at constant *RH*, the differences in
213 breaking stress can be assigned to changes in the film microstructure.

3 Results and Discussion

3.1 Methodology of SAXS data analysis

3.1.1 Sample orientation

Rotation of the film slab allowed to determine two specific clay film orientations (FACE and SIDE) and thus assess the clay platelet anisotropy inside the deposit (Figure 3a). In the FACE orientation, films of clay platelets and spheres feature only an isotropic 2D SAXS pattern (Figure 3b and Figure 3c left), while in the SIDE orientation, the 2D SAXS pattern reveals an anisotropic contribution originating in the 001 reflection of clay platelet stacking (Figure 3b and Figure 3c right). Intensity modulation $I(\theta)$ was obtained from azimuthal signal variation in the SIDE position, at the 001 peak maximum ($q = 0.5\text{Å}^{-1}$) (Figure 3c right). The hk0 reflection possesses an isotropic contribution in the FACE orientation of the films (Figure 3c left), whereas in the SIDE orientation hk0 contribution is anisotropic and is perpendicular to the 001 reflection (Figure 3c right).

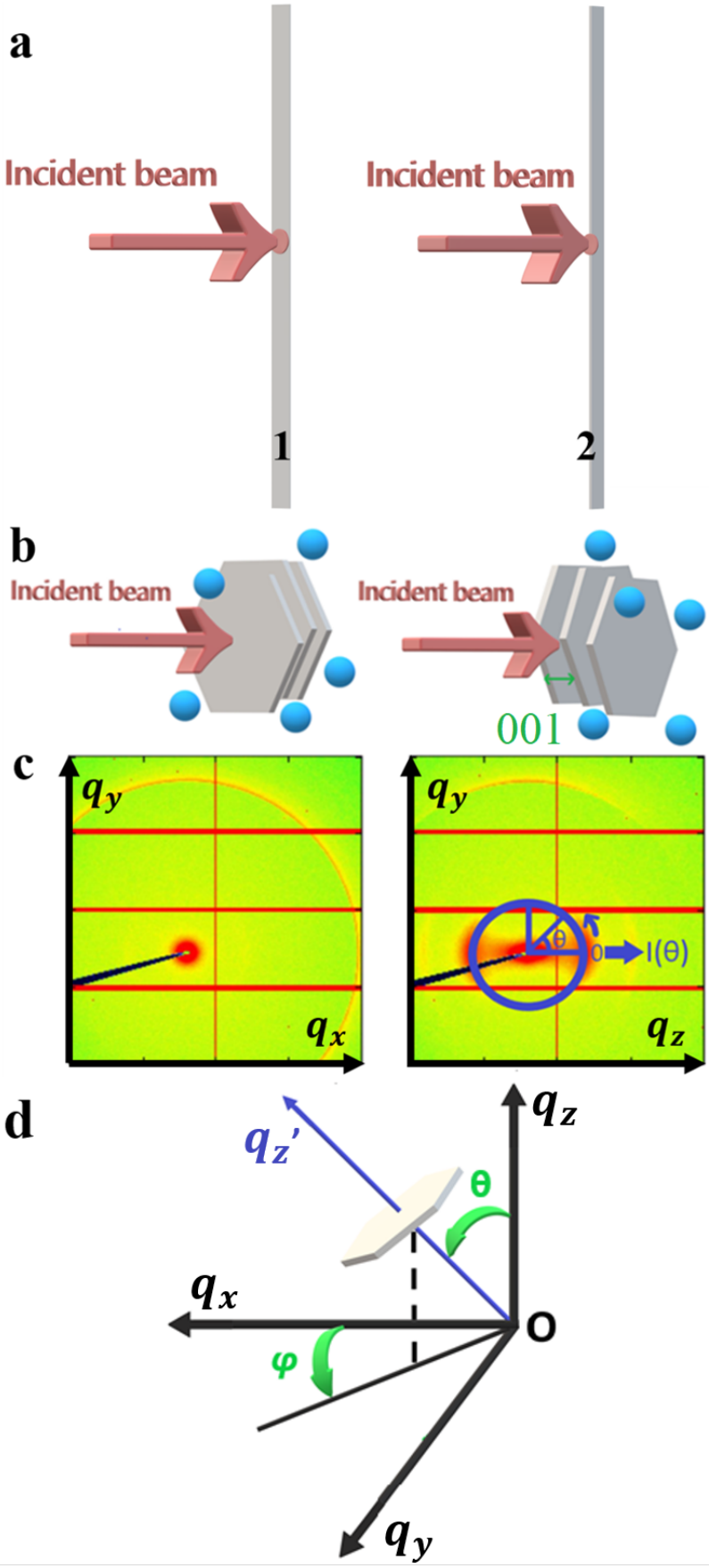
a
Incident beam
Incident beam
1
2
b
Incident beam
Incident beam
001
c
q_y
q_x
q_y
θ
I(θ)
q_z
d
q_z
q_z'
θ
q_x
O
φ
q_y

227

Figure. 3 : Sample under incident beam in SAXS experiment. (a) First sample position (FACE): the incident beam arrives perpendicular to the "face" of the deposit. Second sample position (SIDE): the incident beam arrives from the "side" of the deposit. (b) Schematic drawing of the clay platelets and spheres in the FACE (left) and SIDE (right) sample position. Anisotropy of platelet orientation and the 001 reflection (signature of platelet stacking) are observable in the second (SIDE) position. (c) 2D SAXS patterns on the detector. Intensity modulation $I(\theta)$ was obtained from azimuthal signal variation in the SIDE position, at the 001 peak maximum ($q = 0.5\text{Å}^{-1}$). (d) Clay platelet orientation spherical coordinates in the reciprocal space (qx,qy,qz) .

Clay platelets are a transverse isotropic system (Figure 3d) and the azimuthal profile $I(\theta)$ in the reciprocal space (qx,qy,qz) allows to define and calculate an orientation distribution function (ODF) $f(\theta)$ (Dabat et al., 2019, 2020). The angle φ is chosen uniformly in (0,2π), this range is found in uniaxial nematic phase. ODF features are described by the following equations (Dabat et al., 2019, 2020):

$$f(\theta) \geq 0 \tag{4}$$

$$f(\theta) = f(\pi - \theta) \tag{5}$$

$$\int_0^{\pi} f(\theta)\, sin\,\theta d\theta = 1 \tag{6}$$

$$f(\theta) = \frac{I(\theta)}{\int_0^{\pi} I(\theta) sin\theta\, d\theta} \tag{7}$$

The order parameter $\langle P_2 \rangle$ can then be defined for quantifying clay platelets orientation:

$$\langle P_2 \rangle = \int_0^{\pi} \frac{1}{2}(3cos^2\theta - 1) f(\theta)\, sin(\theta)\, d\theta \tag{8}$$

This order parameter is commonly applied to nematic liquid crystal systems and is also referred to as the nematic order parameter (Hermans and Platzek, 1939). $\langle P_2 \rangle$ varies between $-1/2$ and 1. Particles are randomly oriented when $\langle P_2 \rangle = 0$ and perfectly aligned for $\langle P_2 \rangle = 1$.

Recently a new generalized ODF was developed by (Dabat et al., 2019) for clay phases. This function is based on maximum entropy minimisation and is described by the following equation:

$$f(\theta) = k\, exp\left[\frac{\lambda}{2}(3\, cos^2(\theta - \Psi) - 1) + \frac{0.005\lambda^5}{8}(35\, cos^4(\theta - \Psi) - 30\, cos^2(\theta - \Psi) + 3)\right] \quad (9)$$

Where k is a normalization constant, λ the spreading of ODF and Ψ the deviation angle between detector azimuthal profile reference and ODF maximum. ODF model from eq. (9) was used to fit experimental data and estimate $\langle P_2 \rangle$ value.

In order to isolate the $\langle P_2 \rangle$ parameter corresponding to the clay platelet anisotropic contribution, two methodologies were developed to remove the underlying isotropic contribution (mostly due to scattering signal from the spheres). In the following, S1 beidellite mixed with ludox CL-P at $R_n = 0.3$ is used as an example to explain the two methodologies.

3.1.2 First methodology: background azimuthal profile subtraction

The first methodology used in this work was derived from (Dabat et al., 2020). All the azimuthal profiles were extracted from 2D SAXS patterns in the SIDE orientation, where clay platelet anisotropy is apparent (Figure 3c right). The azimuthal profiles of scattered intensity, $I(\theta)$, necessary to obtain the corrected azimuthal profile used to determine $\langle P_2 \rangle$ are represented in Figure 4a. The background $I_{bkg}(\theta)$ contribution was estimated by averaging azimuthal profiles in the q-range $0.3 - 0.4$ Å^{-1} ($I1_{bkg}(\theta)$) and $0.6 - 0.7$ Å^{-1} ($I2_{bkg}(\theta)$) (Figure 4b). The mean contribution was then subtracted from $I_{stack}(\theta)$ profile at the stacking peak maximum, $q =$ 0.5 Å^{-1} (Figure 4b). The corrected $I_{corr}(\theta)$ profile no longer exhibits non-zero contributions between 60°-120° and 240°-300° and thus contains scattered intensity only from

oriented clay platelets (Figure 4a and b). In the last step, ODF was derived from this corrected $I_{corr}(\theta)$ profile using eq.(7) (Figure 6a).

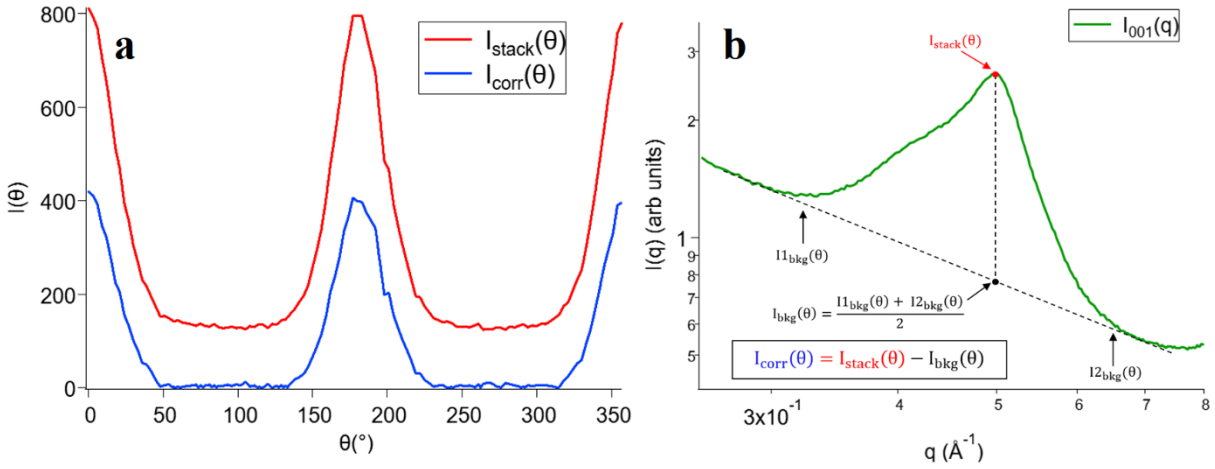

Figure. 4 : First methodology based on isotropic azimuthal profile subtraction. Sample: S1 beidellite + ludox CL-P, $R_n = 0.3$. (a) (red curve) $I_{stack}(\theta)$ at 001 value q = 0.5 Å^{-1}. (blue curve) Obtained $I_{corr}(\theta)$ after subtraction between background $I_{bkg}(\theta)$ and $I_{stack}(\theta)$ at 001. (b) Calculation of background contribution on 001 peak $I(q)$. $I1_{bkg}(\theta)$ is calculated between $q = 0.3 - 0.4$ Å^{-1} and $I2_{bkg}(\theta)$ between $q = 0.6 - 0.7$ Å^{-1}. Background contribution $I_{bkg}(\theta)$ is derived from $I1_{bkg}(\theta)$ and $I2_{bkg}(\theta)$ azimuthal profiles average. Obtained $I(\theta)$ after subtraction between mean $I(\theta)$ and $I(\theta)$ at 001. $I_{stack}(\theta)$ is estimated at 001 maximum peak value $q = 0.5$ Å^{-1}. The corrected $I_{corr}(\theta)$ is the result of the background $I_{bkg}(\theta)$ subtraction to $I_{stack}(\theta)$.

3.1.3 Second methodology: 2D SAXS pattern subtraction

Second methodology was based directly on the 2D SAXS patterns acquired in the FACE and SIDE sample orientations for a given sample (Figure 3c). The 2D SAXS pattern in the FACE orientation was subtracted from the 2D SAXS pattern in the SIDE orientation (Figure 5a). The subtraction between orientations is correct due to the correction and normalization in transmission of SAXS patterns. The resulting 2D SAXS pattern is presented in Figure 5a. Azimuthal profile was then extracted at the 001-value $q = 0.5$Å^{-1} in the subtracted 2D pattern.

Obtained intensity modulation $I(\theta)$ provided only the anisotropic contribution, negligible intensity between 60°-120° and 240°-300° was observed (Figure 5b). The corresponding ODF is represented in Figure 5b.

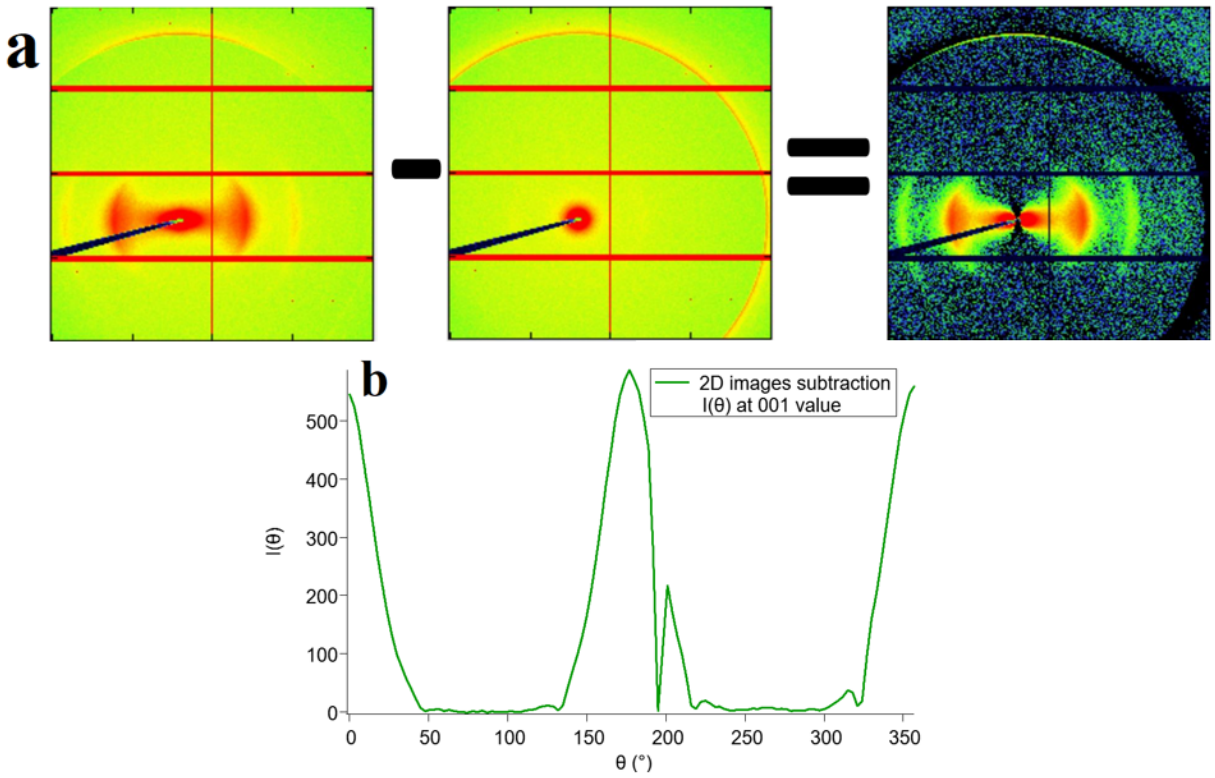

Figure. 5 : Second methodology based on 2D SAXS pattern subtraction. Sample: S1 beidellite + ludox CL-P, $R_n = 0.3$. (a) 2D SAXS patterns from the SIDE and FACE orientation (see Figure 3): pattern for FACE orientation is subtracted from that of the SIDE orientation. (b) Intensity modulation $I(\theta)$ extracted at $q = 0.5$ Å^{-1} on the subtracted 2D pattern.

3.1.4 Fitting of ODF profiles and order parameters

The experimental ODFs resulting from the two above-mentioned methods are displayed in Figure 6. Both ODFs were fitted with eq.(9) and $\langle P_2 \rangle$ was calculated according to eq.(8). The obtained results are almost equivalent as the $\langle P_2 \rangle$ values derived by both methods only differ by 0.02. In the following, for any given system clay platelet orientation is characterised by a single order parameter, calculated as the mean $\langle P_2 \rangle$ value for the two methods. Error bars $\Delta\langle P_2 \rangle$

were estimated as the difference between $\langle P_2 \rangle$ values for the two methods. For the whole series of samples, $\Delta\langle P_2 \rangle$ reached 0.09 at most.

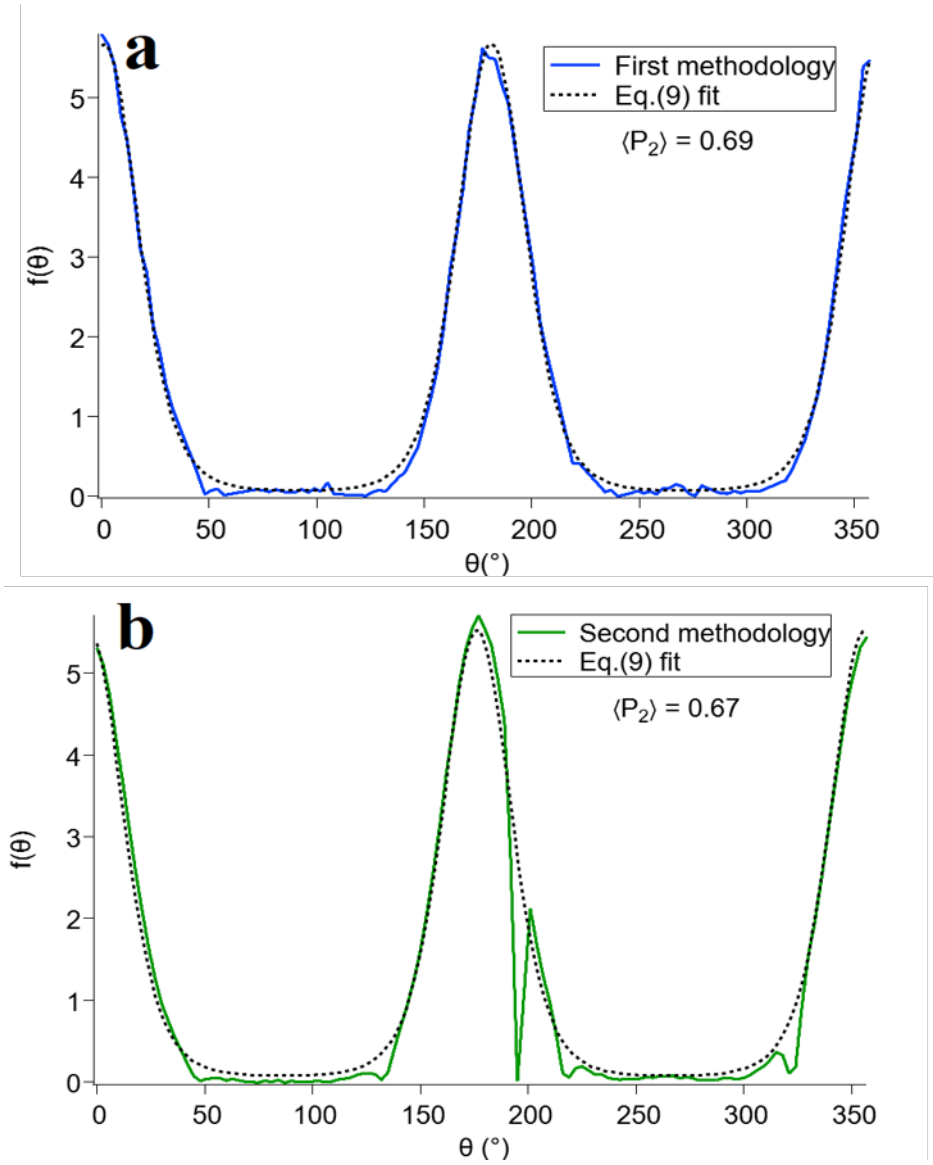

Figure. 6 : ODF fitting by eq. (9) from (Dabat et al., 2019) generalized function. Sample: S1 beidellite + ludox CL-P, $R_n = 0.3$. (a) ODF from the first method "azimuthal profile subtraction", fit with eq. (9) and the derived $\langle P_2 \rangle$ value. (b) ODF from the second method "2D SAXS pattern subtraction", fit with eq. (9) and the derived $\langle P_2 \rangle$ value. Difference between the two methods is $\Delta\langle P_2 \rangle = 0.02$.

3.2 Effect of spheres on clay platelet orientation in self-standing films

3.2.1 Small spheres (~30nm)

Figure 7 presents the evolution of the order parameter $\langle P_2 \rangle$ as a function of R_n for S1 and S3 clay platelets mixed with either positively or negatively charged small spheres. $\langle P_2 \rangle$ for films formed purely of platelets are also displayed in Figure 7 and serve as a reference.

$\langle P_2 \rangle$ values for mixed sphere-platelet films, S1 or S3 with positively or negatively charged spheres, are all similar at the different ratios R_n (Figure 7). The main difference comes from the departure structures of clay-only films. Films formed purely of S3 clay platelets exhibit a very high order parameter, ($\langle P_2 \rangle = 0.97$), in comparison to S1 platelets ($\langle P_2 \rangle = 0.62$) (Figure 7).

Upon addition of positively charged ludox CL-P spheres (Figure 7a), the $\langle P_2 \rangle$ values for S1 platelets do not display any clear evolution and for the highest ratio spheres/platelets ($R_n = 3$), the order parameter value is similar to that obtained in the absence of spheres ($\langle P_2 \rangle = 0.61$). The addition of negatively charged ludox TM-50 spheres appears to lead to a small increase in $\langle P_2 \rangle$ that reach values around 0.75.

In contrast, adding spheres to S3 beidellite has a significant impact on $\langle P_2 \rangle$ values (Figure 7b).[1] The strongly oriented structure of pure S3 beidellite was clearly damaged by both ludox CL-P and ludox TM-50 spheres (Figure 7b). This is more severe with positively charged ludox CL-P spheres ($\langle P_2 \rangle = 0.60$) for $R_n = 3$ than for negatively charged ludox TM-50 ($\langle P_2 \rangle = 0.72$) for $R_n = 3$ (Figure 7b).

[1] (*) Due to experimental constraints, S3 beidellite mixed with ludox TM-50 dispersions were analyzed as films supported on mylar surfaces. In such conditions, due to the parasitic contribution of Mylar to the SAXS patterns, only the first method could be used for determining $\langle P_2 \rangle$. Furthermore, numerous data points were lacking on the data curve $I(\theta)$ because of unfavorable detector position. We then used a slightly different procedure to calculate the ODF. This procedure is described in (Supplementary info 4)

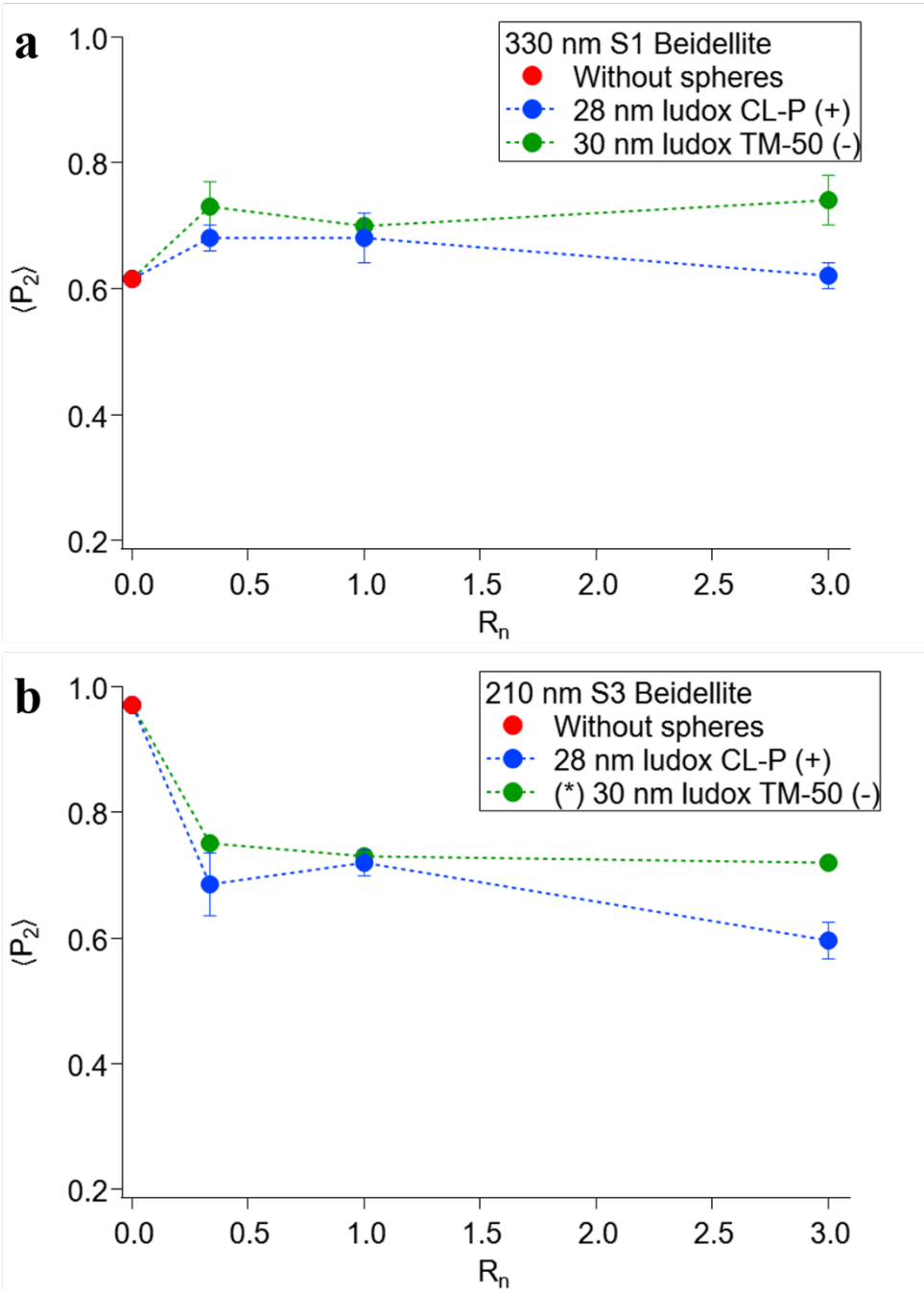

Figure. 7 : Evolution of the $\langle P_2 \rangle$ clay platelet order parameter as a function of sphere/platelet number ratio R_n for small spheres (~30nm). (a) Films of S1 platelets only (●), mixed with small positive spheres (●) and small negative spheres (●). (b) Films of S3 platelets only (●), mixed with small positive spheres (●) and small negative spheres (●).

3.2.2 Large spheres (~300nm)

Figure 8 presents the evolution of the order parameter $\langle P_2 \rangle$ as a function of R_n for S1 and S3 clay platelets mixed with either positively or negatively charged large spheres. $\langle P_2 \rangle$ for

films formed purely of platelets are also displayed in Figure 8 and serve as a reference. Adding positive large spheres to S1 platelets doesn't vary $\langle P_2 \rangle$ values significantly (Figure 8). However, compared to the addition of small spheres, a slight decrease (as opposed to increase) in the order parameter is observed. Regarding S3 clay platelets, large positive spheres strongly reduce the $\langle P_2 \rangle$ values (Figure 8), from 0.97 to 0.32 at the highest R_n ratio. Negatively charge spheres (prepared as films on a mylar support) have equally a strong destructuring effect that seem to happen at higher R_n ratios, contrary to positive spheres (Figure 8)[2].

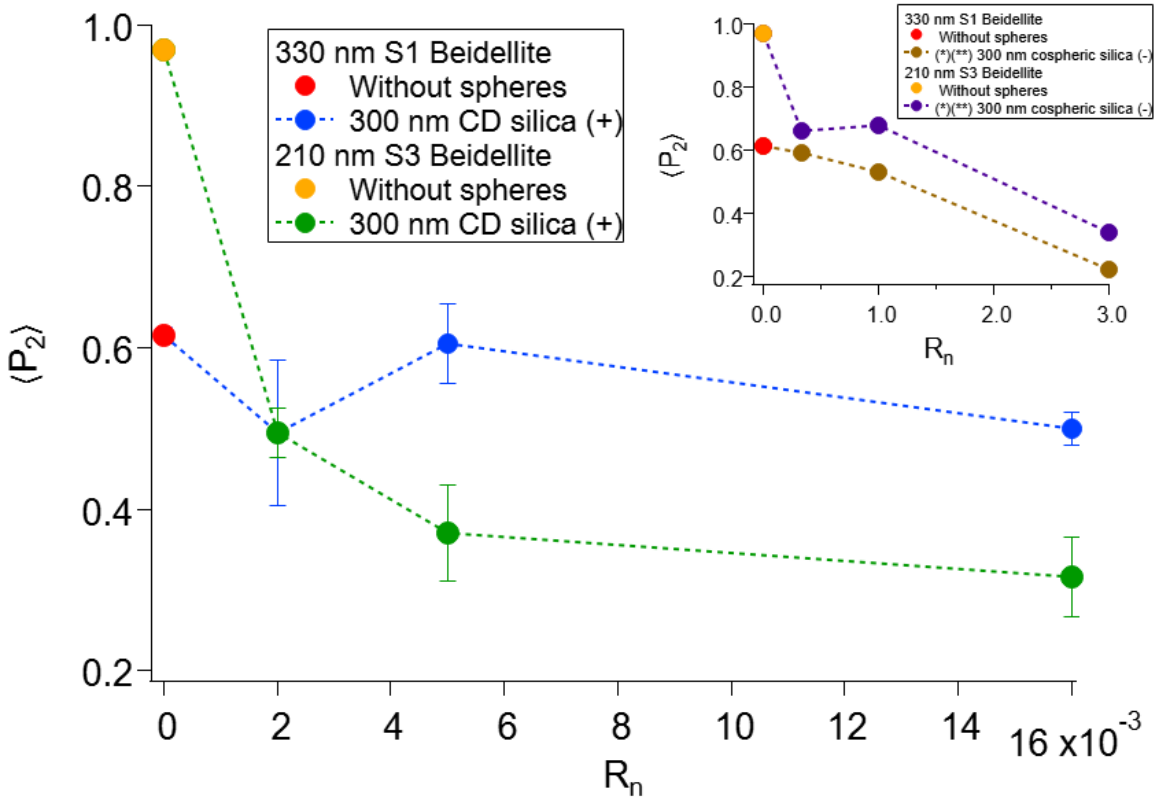

Figure. 8 : Evolution of the $\langle P_2 \rangle$ clay platelet order parameter as a function of sphere/platelet number ratio R_n for large spheres (~300nm). Films of S1/S3 platelets only (●)/(●), S1 platelets mixed with large positive spheres (●) and S3 platelets mixed with large positive spheres (●). (Sub window graph) Films of S1/S3 platelets only (●)/(●), S1 platelets mixed with large negative spheres (●) and S3 platelets mixed with large negative spheres (●).

[2] (**) Negative spheres deposits were produced at the same number ratio Ra_n as small spheres, considering they didn't need to be self-standing films on mylar surfaces (Table 3).

3.3 Link between microscopic structure and macroscopic mechanical properties of the self-standing films

The clay nanoplatelet orientation, characterised by the order parameter $\langle P_2 \rangle$, describes a structural feature at the nm-scale. In an attempt to link this microscopic feature to macroscopic properties of the self-standing films, breaking stress measurements were carried out. Numerous deposits could not be measured due to their brittleness and this was especially the case for films with high R_n ratios and films made of small (S3) platelets and large positive spheres. For brittle films, it was not possible to cut them into the necessary shape for breaking stress measurements (Supplementary info 3 and 5). Several trials were made on different films for the same sample, the number of trials for each sample is summarized in Supplementary info 6. Mean breaking stress values were determined from the average of the different trials and error bars by calculating the difference between the higher and lower obtained values. Figure 9 correlates the breaking stress σ with the order parameter $\langle P_2 \rangle$ for the entire set of the measured films.

Let us consider at first pure clay films. The first point to notice is that the reference system for small (S3) platelets features a mechanical resistance that stands out as a very strong film among all the systems studied (Figure 9a). In particular, its breaking stress is significantly higher than that of the pure film made of large (S1) platelets. We propose that to achieve a mechanically strong film, two parameters are of importance: (a) the number of stacked platelets inside the elementary particle (the clay tactoid) and (b) the alignment between adjacent tactoids. It is possible to evaluate the number of stacked platelets inside tactoids via the width of the 001 stacking peak. According to our measurements (Supplementary info 7), there is no significant difference in the width of the stacking peak between pure S1 and S3 clay films. Consequently, the alignment between adjacent tactoids remains the one significant parameter and, indeed, the pure S3 clay film has a very high $\langle P_2 \rangle$ values of 0.97. The significantly lower $\langle P_2 \rangle$ parameter

383 (0.62) for the S1 pure clay film could be ascribed to flexibility of the larger platelets and/or to
384 size dependent differences in the deposition process itself, as previously reported for
385 vermiculite clays (Hubert et al., 2013; Ferrage et al., 2015).

386 The importance of the $\langle P_2 \rangle$ parameter for the mechanical resistance of the films is further
387 demonstrated by considering the set of S3 films (Figure 9a), for which the addition of both
388 positively and negatively charged spheres leads to a strong decrease $\langle P_2 \rangle$, leading to a drastic
389 drop of the mechanical breaking stress. For the set of S1 films, with positively and negatively
390 charged spheres, the picture is not as clear cut: variation of $\langle P_2 \rangle$ and breaking stress are not as
391 intense (Figure 9b). However, we can distinguish between the effect of positively and
392 negatively charge spheres, the former leading to an increase in the breaking stress, the latter to
393 a decrease of the breaking stress, while all films maintain an intermediate $\langle P_2 \rangle$ value. Thus,
394 alignment of adjacent clay tactoids is of the same order for all systems, but attractive
395 interactions between clays and the added nanospheres may strengthen the contacts between
396 individual clay tactoids, leading to an enhanced mechanical strength of the film on the
397 macroscopic scale. The influence of attractive interactions can also be inferred from the S3
398 systems (Figure 9a). Indeed, films with positively charged spheres also show higher mechanical
399 strength than films with negatively charged spheres.

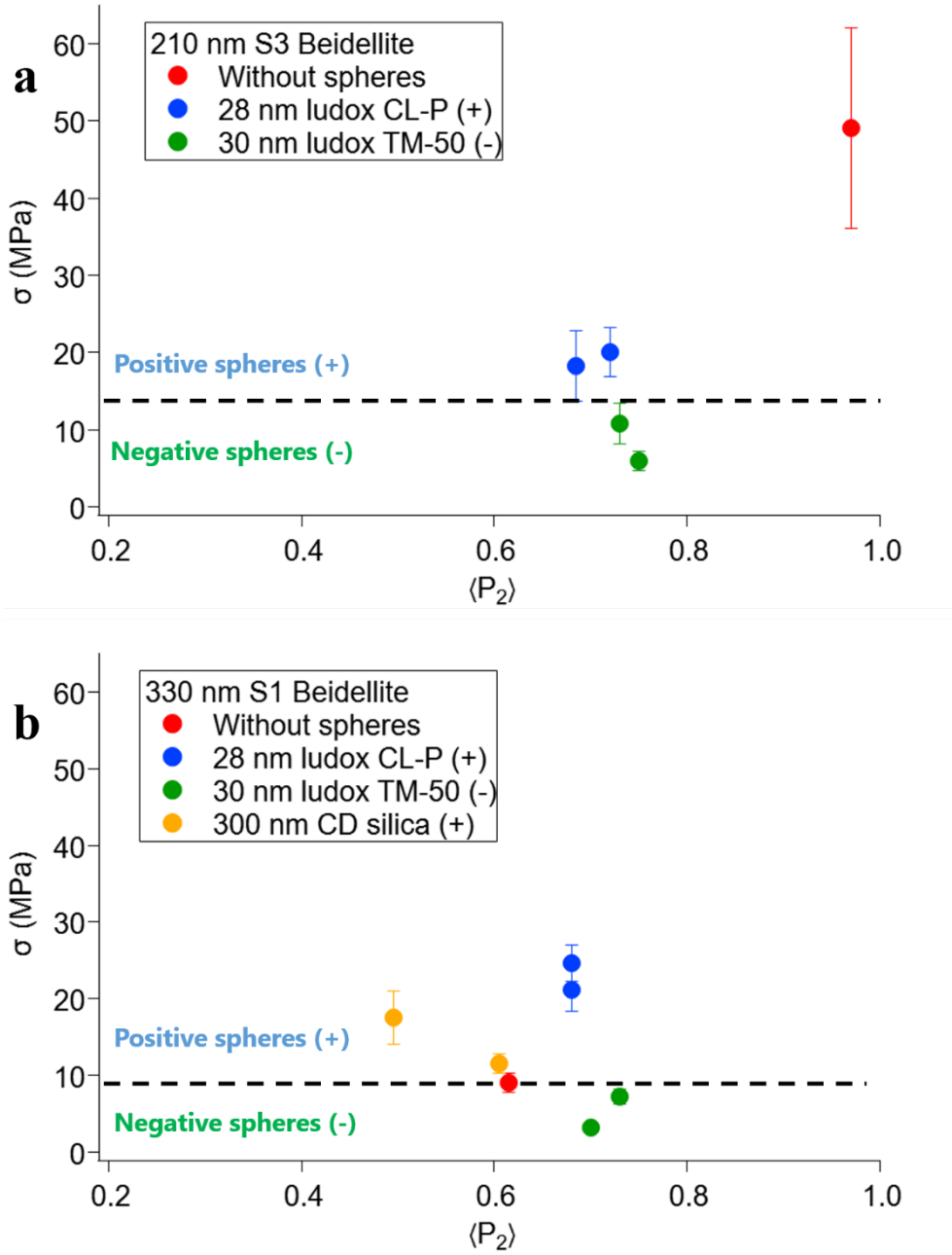

Figure. 9 : Correlating breaking stress measurements, σ, and clay nanoplatelet orientation, as characterised by the order parameter $\langle P_2 \rangle$ determined by SAXS. Mixed sphere/platelet deposits at different R_n ratio for self-standing films form of (a) large (S1) platelets and (b) small (S3) platelets.

Here we have not considered neither the influence of the interlayer cation nor the role of relative humidity. The impact of these two parameters on the mechanical resistance was studied by (Carrier et al., 2016) on montmorillonite films. Effect of interlayer cations on self-

standing film morphology, flexibility and gas barrier property was also noted by (Nam et al., 2009) for montmorillonite. These aspects are directly linked to clay swellability. Exploring various film formation methods is another perspective, as there are different methods to produce self-standing films (Zhou et al., 2011).

4 Conclusion

Clay platelet orientation and mechanical resistance of self-standing films was investigated in the presence of charged spheres of different sizes and surface charge. A SAXS setup and two methodologies of analysis were developed to quantify the clay platelet order parameter $\langle P_2 \rangle$ inside several series of sphere/platelet films. Results between the two methodologies were equivalent.

For films formed of large (S1) clay platelets, sphere addition causes a minor modification of the orientation parameter $\langle P_2 \rangle$. The exception is the addition of a high proportion of large spheres leading to a strong decrease of $\langle P_2 \rangle$, down to 0.2. However, such mixtures can no longer form self-standing films. The situation is very different for small (S3) platelets. The pure (S3) clay system is particularly well-ordered and addition of any type and amount of spheres leads to a significant destructuring of the platelet organisation.

Link between clay platelet orientation at the microscopic scale and macroscopic mechanical resistance was investigated with breaking stress measurements. The well-ordered reference film of pure S3 platelets was by far the strongest film, revealing the importance of degree of orientation for the mechanical properties of the film. Our data suggest that the correlation between orientation and mechanical strength is particularly pronounced in the regime of high order parameter $\langle P_2 \rangle$. Furthermore, the nature of interparticle interactions (attractive/repulsive) has also an effect on the mechanics of the film as, for similar order

parameters, clay films containing positive spheres (large and small) exhibit a stronger mechanical resistance than films containing small negative spheres.

This work opens various perspectives about clay materials and their deposits within the ternary diagram: water-clay-silica. Exploring in detail the relationship between mechanical stress and the order parameter in the high $\langle P_2 \rangle$ range (>0.7) seems particularly relevant, especially in the context of soil crusting. Furthermore, the validity of the calculation of the order parameter $\langle P_2 \rangle$ should be revisited for the case of concentrated systems. Indeed, this order parameter is usually used for dilute nematic systems at thermodynamic equilibrium. For systems outside thermodynamic equilibrium and with a specific morphology, such as self-standing films, the potential role of the film tortuosity at larger scales for the determination of the order parameter needs to be evaluated.

Credit author statement

SV, LM and NM wrote the manuscript and conducted the investigation. SV, PL, LM, TB and NM performed experimental work. SV, PL, LM and NM jointly contributed to the design of the work. PL, LM, PR, OE, TC and NM supervised the work. All the authors contributed to the manuscript revision and have approved the manuscript.

Declaration of competing interest

The authors declare that they have no known competing financial interests or personal relationships that could have appeared to influence the work reported in this paper.

Acknowledgments

The results presented here are part of the PhD thesis of SV funded by the CNRS 80prime program. This research is also part of the Research Joint Laboratory CARMEN (Characterization of Materials for new Energy) between IFPEN, CNRS, University of Strasbourg, ENS Lyon, University of Lyon and Sorbonne University, Paris. The authors acknowledge the SOLEIL synchrotron for awarding the beam time on beamline SWING through the BAG scheme No. 20201118. The authors thank Sirine El Mousli (Phenix, Sorbonne University) and Eric Kohler (IFP Energies Nouvelles) for the TEM and SEM images. The authors are grateful to Matthieu Vandamme (Ecole des Ponts) for the tensile strength setup and discussions about mechanical characterization, José Gomes and Frédéric Gélébart (Phenix, Sorbonne University) for the rotating device and the tools to prepare self-standing films. The authors would also like to thank Eric Ferrage (University of Poitiers) for helpful discussions about clay orientation and order parameter calculation.

Supplementary data

Figure S1 reports the evolution of the zeta potential in function of pH for the silica spheres.

Figure S2 displays the self-standing films and the rotating device.

Figure S3 displays the tensile strength setup and the self-standing film under stress.

Figure S4 reports the methodology to calculate the order parameter for deposits on mylar.

Figure S5 displays self-standing films with brittle structure that were not mechanically characterized.

Table S6 summarizes the number of trials for the different samples characterized with the tensile strength setup.

Figure S7 displays the 001 stacking peak of S1 beidellite and S3 beidellite films without spheres and the width value of the 001 peak for both films.

References

Attou, F., Bruand, A., Le Bissonnais, Y., 1998. Effect of clay content and silt—clay fabric on stability of artificial aggregates. European Journal of Soil Science 49, 569–577. https://doi.org/10.1046/j.1365-2389.1998.4940569.x

Bailey, L., Lekkerkerker, H.N.W., Maitland, G.C., 2015. Smectite clay – inorganic nanoparticle mixed suspensions: phase behaviour and rheology. Soft Matter 11, 222–236. https://doi.org/10.1039/C4SM01717J

Bergaya, F., Theng, B.K.G., Lagaly, G., 2006. Handbook of Clay Science. Elsevier.

Bruand, A., Prost, R., 1988. Analyse minéralogique quantitative d'un échantillon de sol : utilisation des données concernant la composition chimique de l'échantillon. Agronomie 8, 15–22. https://doi.org/10.1051/agro:19880102

Bruand, A., Prost, R., 1987. Effect of water content on the fabric of a soil material: an experimental approach. Journal of Soil Science 38, 461–472. https://doi.org/10.1111/j.1365-2389.1987.tb02281.x

Bruand, A., Tessier, D., Baize, D., 1988. Contribution à l'étude des propriétés de rétention en eau des sols argileux: importance de la prise en compte de l'organisation de la phase argileuse. 7.

Carrier, B., Vandamme, M., Pellenq, R.J.-M., Bornert, M., Ferrage, E., Hubert, F., Van Damme, H., 2016. Effect of Water on Elastic and Creep Properties of Self-Standing Clay Films. Langmuir 32, 1370–1379. https://doi.org/10.1021/acs.langmuir.5b03431

Dabat, T., Hubert, F., Paineau, E., Launois, P., Laforest, C., Grégoire, B., Dazas, B., Tertre, E., Delville, A., Ferrage, E., 2019. A general orientation distribution function for clay-rich media. Nat Commun 10, 5456. https://doi.org/10.1038/s41467-019-13401-0

Dabat, T., Porion, P., Hubert, F., Paineau, E., Dazas, B., Grégoire, B., Tertre, E., Delville, A., Ferrage, E., 2020. Influence of preferred orientation of clay particles on the diffusion of water in kaolinite porous media at constant porosity. Applied Clay Science 184, 105354. https://doi.org/10.1016/j.clay.2019.105354

Doshi, N., Cinacchi, G., van Duijneveldt, J.S., Cosgrove, T., Prescott, S.W., Grillo, I., Phipps, J., Gittins, D.I., 2011. Structure of colloidal sphere–plate mixtures. J. Phys.: Condens. Matter 23, 194109. https://doi.org/10.1088/0953-8984/23/19/194109

Ferrage, E., Hubert, F., Tertre, E., Delville, A., Michot, L.J., Levitz, P., 2015. Modeling the arrangement of particles in natural swelling-clay porous media using three-dimensional packing of elliptic disks. Phys. Rev. E 91, 062210. https://doi.org/10.1103/PhysRevE.91.062210

Fiès, J.C., Stengel, P., 1984. Relations entre la constitution granulométrique et minéralogique et les caractéristiques de l'espace poral des sols 10.

Geoffroy, V., Dazas, B., Ferrage, E., Tertre, E., Boissard, C., Berenguer, F., Michot, L.J., van Oort, F., Hubert, F., 2022. Soil crusting: new insight from synchrotron 2D-µXRD mapping of clay-particle orientation and mineralogy ». Geoderma 2022.

Hermans, P.H., Platzek, P., 1939. Das Lichtbrechungsvermögen der Cellulose in Funktion des Quellungsgrades. Recueil des Travaux Chimiques des Pays-Bas 58, 1001–1007. https://doi.org/10.1002/recl.19390581112

Hilhorst, J., Meester, V., Groeneveld, E., Dhont, J.K.G., Lekkerkerker, H.N.W., 2014. Structure and Rheology of Mixed Suspensions of Montmorillonite and Silica Nanoparticles. J. Phys. Chem. B 118, 11816–11825. https://doi.org/10.1021/jp504217m

Housni, S., Abramson, S., Guigner, J.-M., Levitz, P., Michot, L., 2020. Flocculation and magnetically-assisted sedimentation of size-sorted beidellite platelets mixed with maghemite nanoparticles. Nano Research 13, 3001–3011. https://doi.org/10.1007/s12274-020-2964-9

Hubert, F., Bihannic, I., Prêt, D., Tertre, E., Nauleau, B., Pelletier, M., Demé, B., Ferrage, E., 2013. Investigating the Anisotropic Features of Particle Orientation in Synthetic Swelling Clay Porous Media. Clays and Clay Minerals 61, 397–415. https://doi.org/10.1346/CCMN.2013.0610501

Landman, J., Paineau, E., Davidson, P., Bihannic, I., Michot, L.J., Philippe, A.-M., Petukhov, A.V., Lekkerkerker, H.N.W., 2014. Effects of Added Silica Nanoparticles on the Nematic Liquid Crystal Phase Formation in Beidellite Suspensions. J. Phys. Chem. B 118, 4913–4919. https://doi.org/10.1021/jp500036v

Michot, L.J., Bihannic, I., Porsch, K., Maddi, S., Baravian, C., Mougel, J., Levitz, P., 2004. Phase Diagrams of Wyoming Na-Montmorillonite Clay. Influence of Particle Anisotropy. Langmuir 20, 10829–10837. https://doi.org/10.1021/la0489108

Nam, H.-J., Ebina, T., Mizukami, F., 2009. Formability and properties of self-standing clay film by montmorillonite with different interlayer cations. Colloids and Surfaces A: Physicochemical and Engineering Aspects 346, 158–163. https://doi.org/10.1016/j.colsurfa.2009.06.009

Paineau, E., Antonova, K., Baravian, C., Bihannic, I., Davidson, P., Dozov, I., Impéror-Clerc, M., Levitz, P., Madsen, A., Meneau, F., Michot, L.J., 2009. Liquid-Crystalline Nematic Phase in Aqueous Suspensions of a Disk-Shaped Natural Beidellite Clay. J. Phys. Chem. B 113, 15858–15869. https://doi.org/10.1021/jp908326y

Paineau, E., Bihannic, I., Baravian, C., Philippe, A.-M., Davidson, P., Levitz, P., Funari, S.S., Rochas, C., Michot, L.J., 2011. Aqueous Suspensions of Natural Swelling Clay Minerals. 1. Structure and Electrostatic Interactions. Langmuir 27, 5562–5573. https://doi.org/10.1021/la2001255

Rozenbaum, O., Bruand, A., Le Trong, E., 2012. Soil porosity resulting from the assemblage of silt grains with a clay phase: New perspectives related to utilization of X-ray synchrotron computed microtomography. Comptes Rendus Geoscience 344, 516–525. https://doi.org/10.1016/j.crte.2012.09.004

Soil Survey Staff. 1999. Soil taxonomy: A basic system of soil classification for making and interpreting soil surveys. 2nd edition. Natural Resources Conservation Service. U.S. Department of Agriculture Handbook 436., 1999.

Stoops, G., Jongerius, A., 1975. Proposal for a micromorphological classification of soil materials. I. A classification of the related distributions of fine and coarse particles. Geoderma 13, 189–199. https://doi.org/10.1016/0016-7061(75)90017-8

Velde, B., 1992. Clays as minerals, in: Velde, B. (Ed.), Introduction to Clay Minerals: Chemistry, Origins, Uses and Environmental Significance. Springer Netherlands, Dordrecht, pp. 41–100. https://doi.org/10.1007/978-94-011-2368-6_3

Zhou, C.-H., Shen, Z.-F., Liu, L.-H., Liu, S.-M., 2011. Preparation and functionality of clay-containing films. J. Mater. Chem. 21, 15132. https://doi.org/10.1039/c1jm11479d